ELSEVIER

Comput. Methods Appl. Mech. Engrg. 187 (2000) 137–159

Computer methods in applied mechanics and engineering

www.elsevier.com/locate/cma

Implementation of exact non-reflecting boundary conditions in the finite element method for the time-dependent wave equation

Lonny L. Thompson *, Runnong Huan

Department of Mechanical Engineering, 102 Fluor Daniel Building, Clemson University, Clemson, SC 29634, USA

Received 13 February 1998

Abstract

When solving the wave equation in infinite regions using finite element methods, the domain must be truncated. We investigate the accuracy of time-dependent non-reflecting boundary conditions (NRBC) derived in Grote, Keller (1995), when implemented in the finite element method. The NRBC annihilate the first N wave harmonics on a spherical truncation boundary. High-order temporal derivatives are formulated as a system of first-order ordinary differential equations. Several versions of implicit and explicit multi-step, time-integration schemes are presented for solution of the finite element equations concurrently with the first-order system appearing in the NRBC. An alternative scaling of the boundary variables is introduced which leads to a well-conditioned coefficient matrix. Although the boundary conditions are global over the boundary, when implemented in the finite element method, they only require inner products of spherical harmonics within the force vector, and as a result, they are easy to implement and do not disturb the banded/sparse structure of the matrix equations. Several numerical examples are presented which demonstrate the improvement in accuracy over standard finite element methods.

1. Introduction

When domain based computational methods such as finite element methods are used to model infinite domains, accurate non-reflecting boundary conditions (NRBC), infinite elements, or absorbing layers, are required on an artificial truncation boundary Γ that surrounds the source of radiation or scattering [1]. If the form of the boundary treatment is over-simplified, spurious reflected waves can be generated at the artificial boundary, which can substantially degrade the accuracy of the numerical solution. For example the simple 'spherical-damper' on Γ,

$$\frac{\partial \phi}{\partial r} + \frac{1}{c}\frac{\partial \phi}{\partial t} + \frac{1}{R}\phi = 0, \tag{1}$$

where $\phi(x,t)$ is the solution to the scalar wave equation, R the radius of a spherical artificial boundary Γ, and c the wave speed, while exact for all uniform spherical outgoing waves, exhibits significant spurious reflection for higher-order wave harmonics, especially as the position of Γ approaches the source of radiation or scattering [2,3], and for low frequency (long wavelength) components [4]. If accurate non-reflecting (radiation) boundary conditions are applied to this boundary, the finite computational region can be reduced in size and the truncation boundary moved closer the radiator/scatterer, so that fewer finite elements are needed, resulting in considerable cost savings.

* Corresponding author.

0045-7825/00/$ - see front matter
PII: S0045-7825(99)00114-0

In the frequency domain, it is well known that an exact NRBC applied to a separable truncation boundary is available through the Dirichlet-to-Neumann (DtN) map [5,6]. The DtN map is a nonlocal (integral) operator composed of a series of wave harmonics relating DtN data on the truncation boundary. The DtN map is easily implemented in the finite element method as a 'natural' boundary condition using standard C^0 continuous interpolation functions in the frequency domain.

Time-dependent NRBC based on the DtN map which match the first N wave harmonics on a spherical boundary have been derived in Refs. [4,7,8]. Two alternative sequences of NRBC have been derived, the first involves temporal derivatives while retaining a spatial integral (local in time and non-local in space version), while the second involves both temporal and spatial derivatives (local in time and local in space version). As the order of these local NRBC are raised they become increasingly difficult to implement directly in standard semidiscrete finite element formulations due to the occurrence of high-order time-derivatives on the truncation boundary. In practice, this has limited their use to second-order when implemented with standard finite element methods [3].

Recently, following a suggestion by Buneman, Grote and Keller [8] have shown how to replace the high-order derivatives appearing in the NRBC with a system of linear first-order differential equations in time. By reducing the time-derivatives to first-order, the resulting form of the NRBC is easily combined with standard finite difference methods and finite element methods [9]. In Ref. [9], Grote and Keller show how to combine the NRBC with the semidiscrete finite element formulation and give numerical examples implemented using an explicit finite difference method.

In this work, examples of finite element computations using a modified version of the exact NRBC are reported. Several versions of implicit and explicit multi-step, time-integration schemes are presented for solution of the finite element semidiscrete equations concurrently with the system of first-order differential equations appearing in the NRBC. In Ref. [8] derivation of the NRBC relied on an integral transform of radial harmonics. We show that the NRBC can be derived in a straight-forward approach based on a recurrence relation given by Lamb [10], which does not require the use of an integral equation. In order to improve the condition number of the coefficient matrix appearing in the discrete form of the NRBC, we introduce an alternative scaling of the solution variables than used in Ref. [8]. Several numerical experiments are performed to assess the accuracy and convergence properties of the NRBC when implemented in the finite element method. Comparisons are made to a local second-order boundary condition [2,3]. Two model problems are studied, in the first we investigate the ability of the NRBC to annihilate high-order spherical harmonics on the truncation boundary, and in the second we investigate the accuracy of the NRBC for a challenging test problem of radiation from a piston on a sphere.

2. Exact non-reflecting boundary condition

In this section we show how the NRBC follows directly from a recurrence relation given by Ref. [10]. We consider time-dependent scattering/radiation in an infinite domain. The unbounded region is truncated by an artificial boundary Γ, and we denote by Ω the finite computational domain inside Γ. The boundary Γ is restricted to be a sphere of radius R. In Ω we assume the solution $\phi(x,t)$ is governed by the non-homogenous wave equation:

$$\nabla^2\phi - \frac{1}{c^2}\frac{\partial^2\phi}{\partial t^2} = -f \qquad \text{in } \Omega \times]0,T[, \tag{2}$$

$$\phi(x,0) = \phi_0, \quad \dot{\phi}(x,0) = \dot{\phi}_0, \quad x \in \Omega. \tag{3}$$

At $t = 0$, the source $f(x,t)$ and initial data are assumed to be confined to the computational region Ω, so that in the exterior domain $\mathscr{D}$, i.e., the region outside Γ, the scalar field $\phi(x,t)$ satisfies the homogeneous form of the wave equation,

$$\nabla^2\phi - \frac{1}{c^2}\frac{\partial^2\phi}{\partial t^2} = 0 \qquad \text{in } \mathscr{D} \times]0,T[, \tag{4}$$

$$\phi(x,0)=0, \quad \dot{\phi}(x,0)=0, \quad x\in\mathscr{D}. \tag{5}$$

A general solution to Eq. (4) in spherical coordinates (r,θ,φ) is

$$\phi(r,\theta,\varphi,t)=\sum_{n=0}^{\infty}\sum_{m=-n}^{n}\phi_{nm}(r,t)Y_{nm}(\theta,\varphi), \tag{6}$$

where Y_{nm} are orthogonal spherical harmonics normalized on the unit sphere

$$Y_{nm}(\theta,\varphi)=[(2n+1)(n-|m|)!/4\pi(n+|m|)!]^{1/2}\mathrm{e}^{\mathrm{i}m\varphi}P_n^{|m|}(\cos\theta). \tag{7}$$

The time-dependent radial functions $\phi_{nm}(r,t)$ are obtained by multiplying Eq. (6) by the complex conjugate of Y_{nm}, denoted Y_{nm}^*, and integrating over the unit surface, i.e., forming the inner product,

$$\phi_{nm}(r,t)=(\phi,Y_{nm})\equiv\int_0^{2\pi}\int_0^{\pi}Y_{nm}^*(\theta,\varphi)\phi(r,\theta,\varphi,t)\sin\theta\,\mathrm{d}\theta\,\mathrm{d}\varphi, \tag{8}$$

The radial functions $\phi_{nm}(r,t)$ satisfy the following equation and initial conditions:

$$L_n[\phi_{nm}]\equiv\left[\frac{1}{c^2}\frac{\partial^2}{\partial t^2}-\frac{\partial^2}{\partial r^2}-\frac{2}{r}\frac{\partial}{\partial r}+\frac{n(n+1)}{r^2}\right]\phi_{nm}(r,t)=0, \quad r\geqslant R, \tag{9}$$

$$\phi_{nm}(r,0)=0, \quad \dot{\phi}_{nm}(r,0)=0, \quad r\geqslant R. \tag{10}$$

The presence of the index m in ϕ_{nm} for $|m|\leqslant n, n=0,\ldots,\infty$ denotes different members in the solution family of Eq. (9). For clarity, in the discussion below, the index m will be suppressed, i.e. we define $\phi_n\equiv\phi_{nm}$.

Based on a result given by Lamb [10], ϕ_{nm} satisfies the recurrence relation

$$\phi_n=\left(\frac{\partial}{\partial r}-\frac{n-1}{r}\right)\phi_{n-1}, \tag{11}$$

where ϕ_{n-1} is the solution to $L_{n-1}[\phi_{n-1}]=0$.

The following equality can be easily verified,

$$L_n\left[\left(\frac{\partial}{\partial r}-\frac{n-1}{r}\right)\phi_{n-1}\right]=\left(\frac{\partial}{\partial r}-\frac{n-1}{r}\right)L_{n-1}[\phi_{n-1}]. \tag{12}$$

Since ϕ_{n-1} satisfies $L_{n-1}[\phi_{n-1}]=0$, then it follows from Eq. (12) that $(\partial/\partial r-(n-1)/r)\phi_{n-1}$ satisfies $L_n[\phi_n]=0$, which implies (11).

Recursive use of Eq. (11) gives

$$\begin{aligned}\phi_n&=\left(\frac{\partial}{\partial r}-\frac{n-1}{r}\right)\phi_{n-1}\\&=\left(\frac{\partial}{\partial r}-\frac{n-1}{r}\right)\left(\frac{\partial}{\partial r}-\frac{n-2}{r}\right)\cdots\left(\frac{\partial}{\partial r}-\frac{1}{r}\right)\frac{\partial}{\partial r}\phi_0\\&=\prod_{j=1}^{n}\left(\frac{\partial}{\partial r}-\frac{j-1}{r}\right)\phi_0.\end{aligned} \tag{13}$$

The function $\phi_0\equiv\phi_{00}$ satisfies Eq. (9) with $n=0$, i.e.

$$\left[\frac{1}{c^2}\frac{\partial^2}{\partial t^2}-\frac{\partial^2}{\partial r^2}-\frac{2}{r}\frac{\partial}{\partial r}\right]\phi_0(r,t)=0. \tag{14}$$

Using the transformation $\phi_0 = r^{-1}v$, Eq. (14) reduces to the one-dimensional wave equation in r

$$\left[\frac{1}{c^2}\frac{\partial^2}{\partial t^2} - \frac{\partial^2}{\partial r^2}\right] v = 0. \tag{15}$$

For outgoing waves, general solutions of Eq. (15) take the form $v_n(r-ct)$. Using this result in Eq. (13) gives,

$$\phi_n = \prod_{j=1}^{n}\left(\frac{\partial}{\partial r} - \frac{j-1}{r}\right)\frac{v_n(r-ct)}{r}, \quad n \geqslant 1, \ \ |m| \leqslant n. \tag{16}$$

Expanding (16) leads to an operator form involving nth-order radial derivatives. For the first several terms in Eq. (16) we have,

$$\phi_1 = \frac{\partial}{\partial r}\frac{v_1(r-ct)}{r} = \frac{1}{r}\frac{\partial v_1}{\partial r} - \frac{v_1}{r^2}, \tag{17}$$

$$\phi_2 = \left(\frac{\partial}{\partial r} - \frac{1}{r}\right)\frac{\partial}{\partial r}\frac{v_2(r-ct)}{r} = \frac{1}{r}\frac{\partial^2 v_2}{\partial r^2} - \frac{3}{r^2}\frac{\partial v_2}{\partial r} + \frac{3v_2}{r^3}, \tag{18}$$

$$\phi_3 = \left(\frac{\partial}{\partial r} - \frac{2}{r}\right)\left(\frac{\partial}{\partial r} - \frac{1}{r}\right)\frac{\partial}{\partial r}\frac{v_3(r-ct)}{r} \tag{19}$$

$$= \frac{1}{r}\frac{\partial^3 v_3}{\partial r^3} - \frac{6}{r^2}\frac{\partial^2 v_3}{\partial r^2} + \frac{15}{r^3}\frac{\partial v_3}{\partial r} - \frac{15}{r^4}v_3. \tag{20}$$

By induction, the nth term takes the form

$$\phi_{nm} = \prod_{j=1}^{n}\left(\frac{\partial}{\partial r} - \frac{j-1}{r}\right)\frac{v_{nm}(r-ct)}{r} = \sum_{j=0}^{n}\frac{(-1)^j}{r^{j+1}}a_n^j\frac{\partial^{n-j}}{\partial r^{n-j}}v_{nm}(r-ct). \tag{21}$$

The coefficients

$$a_n^j = \frac{(n+j)!}{2^j j!(n-j)!} \tag{22}$$

are obtained from an evolution formula derived by equating coefficients of the expression for ϕ_n with ϕ_{n+1}, see Appendix. The result (21) is the same equation given in Ref. [8], Lemma 7.1, and proved by an alternate method involving an integral operator.

The expression for ϕ_{nm} given in Eq. (21) involves high-order radial derivatives which are difficult to implement in a numerical method. Making use of the special property of the wave functions $v_{nm}(r-ct)$

$$(-1)^k\frac{\partial^k}{\partial r^k}v_{nm}(r-ct) = \frac{1}{c^k}\frac{\partial^k}{\partial t^k}v_{nm}(r-ct), \tag{23}$$

the radial derivatives in Eq. (21) are replaced with time-derivatives to obtain

$$\phi_{nm}(r,t) = (-1)^n\sum_{j=0}^{n}\frac{1}{c^{n-j}}\frac{a_n^j}{r^{j+1}}\frac{\partial^{n-j}}{\partial t^{n-j}}v_{nm}(r-ct). \tag{24}$$

Following Grote and Keller, we apply the 'spherical damper', denoted B_1,

$$B_1[\phi_{nm}] \equiv \left(\frac{\partial}{\partial r} + \frac{1}{c}\frac{\partial}{\partial t} + \frac{1}{r}\right)\phi_{nm}(r,t), \tag{25}$$

to Eq. (24), and use Eq. (23) with $k = 1$ to eliminate the radial derivative in favor of a time-derivative to obtain,

$$\left(\frac{\partial}{\partial r}+\frac{1}{c}\frac{\partial}{\partial t}+\frac{1}{r}\right)\phi_{nm}(r,t)=\frac{(-1)^{n+1}}{r}\sum_{j=1}^{n}\frac{j}{c^{n-j}}\frac{a_n^j}{r^{j+1}}\frac{\partial^{n-j}}{\partial t^{n-j}}v_{nm}(r-ct). \tag{26}$$

Multiplying Eq. (26) by $Y_{nm}(\theta,\varphi)$, summing over n and m, setting $r=R$ and using Eq. (6) gives

$$B_1[\phi(R,\theta,\varphi,t)]=-\frac{1}{R}\sum_{n=1}^{\infty}\sum_{m=-n}^{n}Y_{nm}(\theta,\varphi)\sum_{j=1}^{n}\frac{j}{c^{n-j}}\frac{a_n^j}{R^j}\frac{\mathrm{d}^{n-j}}{\mathrm{d}t^{n-j}}w_{nm}(t), \tag{27}$$

where

$$w_{nm}(t)=(-1)^n v_{nm}(R-ct)/R. \tag{28}$$

Eq. (27) is the exact NRBC given in [8], Theorem 7.1, with the functions w_{nm} rescaled by $(-1)^n/R$. The B_1 operator is exact for the breathing mode $\phi_{00}=v_n(r-ct)/r$ and annihilates any spherically symmetric outgoing wave such as the leading term $1/r$, of the multipole expansion [2,15], for $\phi(x,t)$

$$\phi(r,\theta,\varphi,t)=\sum_{j=1}^{\infty}\frac{g_j(r-ct,\theta,\varphi)}{r^j}. \tag{29}$$

When B_1 is applied to Eq. (29), then

$$B_1\phi=\mathrm{O}\left(\frac{1}{r^3}\right) \tag{30}$$

which shows that the boundary condition $B_1\phi=0$ is only approximate for modes $n\geqslant 1$. The summation over the series in Eq. (27) may be viewed as an extension of the B_1 operator. In computation, the sum over n in Eq. (27) is truncated at a finite value $N\geqslant 1$. The modes $n\leqslant N$ will be represented exactly. The boundary condition (27) approximates the modes beyond the point of truncation, i.e. it reduces to $B_1\phi=0$ at $r=R$, for the modes $n>N$.

The functions $w_{nm}(t)$ are obtained from Eq. (24) evaluated at $r=R$,

$$\phi_{nm}(R,t)=\sum_{j=0}^{n}\frac{1}{c^{n-j}}\frac{a_n^j}{R^j}\frac{\mathrm{d}^{n-j}}{\mathrm{d}t^{n-j}}w_{nm}(t). \tag{31}$$

Using $a_n^0=1$ and rearranging Eq. (31) we find that $w_{nm}(t)$ is the solution of a linear ordinary differential equation of order n in the dependent variable $w_{nm}(t)$, with non-homogenous term $\phi_{nm}(R,t)=(\phi,Y_{nm})(R,t)$,

$$\frac{1}{c^n}\frac{\mathrm{d}^n}{\mathrm{d}t^n}w_{nm}(t)=-\sum_{j=1}^{n}\frac{1}{c^{n-j}}\frac{a_n^j}{R^j}\frac{\mathrm{d}^{n-j}}{\mathrm{d}t^{n-j}}w_{nm}(t)+\phi_{nm}(R,t). \tag{32}$$

The initial conditions on $w_{nm}(t)$ are obtained from Eq. (10)

$$w_{nm}(0)=\frac{\mathrm{d}}{\mathrm{d}t}w_{nm}(0)=\cdots=\frac{\mathrm{d}^{n-1}}{\mathrm{d}t^{n-1}}w_{nm}(0)=0. \tag{33}$$

The right side of Eq. (27) involves $w_{nm}(t)$, the solution to Eqs. (32) and (33), and its time-derivatives up to order $n-1$. The nth-order differential equation (32) is reduced to a system of first-order differential equations for $w_{nm}(t)$ and its derivatives up to order $n-1$ by defining the vector function,

$$\boldsymbol{z}_{nm}(t)=\left[b_n^1\frac{\mathrm{d}^{n-1}}{\mathrm{d}t^{n-1}}w_{nm}(t),b_n^2\frac{\mathrm{d}^{n-2}}{\mathrm{d}t^{n-2}}w_{nm}(t),\ldots,b_n^n w_{nm}(t)\right]^{\mathrm{T}}, \tag{34}$$

$$z_{nm}^i(t)=b_n^i\frac{\mathrm{d}^{n-i}}{\mathrm{d}t^{n-i}}w_{nm}(t),\quad i=1,\ldots,n. \tag{35}$$

To eliminate the large a_n^j and R^j that appear in Eqs. (27) and (32) we have scaled w_{nm} and its $n-1$ derivatives by,

$$b_n^i = \frac{1}{R^{i-1}c^{n-i}}\frac{a_n^i}{a_n^1}. \tag{36}$$

This scaling is different from that used by Grote and Keller [8], where the following alternative scaling was used:

$$\tilde{b}_n^i = \frac{1}{c^{n-i}}\frac{a_n^i}{a_n^1}. \tag{37}$$

The functions $z_{nm}^i(t)$ in Eq. (35) are the terms on the right side of Eq. (27),

$$B_1\phi = -\frac{1}{R}\sum_{n=1}^{\infty}\sum_{m=-n}^{n} Y_{nm}\sum_{j=1}^{n} e_n^j z_{nm}^j(t) \quad \text{on } \Gamma\times]0,T[, \tag{38}$$

where

$$e_n^j = \frac{ja_n^1}{R} = n(n+1)j/2R \quad j=1,\ldots,n \tag{39}$$

or in vector form with coefficient vectors $\boldsymbol{e}_n = \{e_n^j\}$

$$B_1\phi = -\frac{1}{R}\sum_{n=1}^{\infty}\sum_{m=-n}^{n} (\boldsymbol{e}_n\cdot\boldsymbol{z}_{nm})Y_{nm}(\theta,\varphi) \quad \text{on } \Gamma\times]0,T[. \tag{40}$$

Eq. (40) is the exact NRBC written in a form with only first-order derivatives in r and t. The vector functions $\boldsymbol{z}_{nm}(t)$ are solutions to the system of first-order differential equations obtained by replacing $w_{nm}(t)$ in Eq. (32) and its time-derivatives with $\boldsymbol{z}_{nm}(t)$.

Differentiating Eq. (35) gives,

$$\frac{\mathrm{d}z_{nm}^i(t)}{\mathrm{d}t} = b_n^i\frac{\mathrm{d}^{n-i+1}}{\mathrm{d}t^{n-i+1}}w_{nm}(t), \quad i=1,\ldots,n. \tag{41}$$

For $i=1$,

$$\frac{\mathrm{d}z_{nm}^1(t)}{\mathrm{d}t} = b_n^1\frac{\mathrm{d}^n}{\mathrm{d}t^n}w_{nm}(t) = \frac{1}{c^{n-1}}\frac{\mathrm{d}^n}{\mathrm{d}t^n}w_{nm}(t). \tag{42}$$

Using definition (35) and Eq. (42) in (32), the nth-order differential equation in $w_{nm}(t)$ is reduced to the following first-order equation in $z_{nm}(t)$,

$$\frac{\mathrm{d}z_{nm}^1(t)}{\mathrm{d}t} = \sum_{j=1}^{n} A_n^{1j}z_{nm}^j(t) + c\phi_{nm}(t), \quad i=1, \tag{43}$$

where

$$A_n^{1j} = -\frac{c}{R}a_n^1 = -\frac{n(n+1)c}{2R}. \tag{44}$$

Combining Eqs. (35) and (41), gives the remaining differential equations,

$$\frac{\mathrm{d}z_{nm}^i(t)}{\mathrm{d}t} = \beta_n^i z_{nm}^{i-1}(t), \quad i=2,\ldots,n, \tag{45}$$

where

$$\beta_n^i = \frac{b_n^i}{b_n^{i-1}} = \frac{c}{R}\frac{a_n^i}{a_n^{i-1}} = \frac{c(n+i)(n-i+1)}{2iR}. \tag{46}$$

The system of equations (43) and (45) may be written in standard matrix form as,

$$\frac{\mathrm{d}}{\mathrm{d}t}\boldsymbol{z}_{nm}(t) = \boldsymbol{A}_n\boldsymbol{z}_{nm}(t) + \boldsymbol{\Phi}_{nm}(t) \tag{47}$$

with homogeneous initial conditions $\boldsymbol{z}_{nm}(0) = 0$, obtained from Eq. (33).

In Eq. (47), the $n \times n$ matrices $\boldsymbol{A}_n = \left[A_n^{ij}\right]$, take the form

$$\boldsymbol{A}_n = \frac{c}{R}\begin{bmatrix} \frac{-n(n+1)}{2} & \frac{-n(n+1)}{2} & \cdots & \frac{-n(n+1)}{2} & \frac{-n(n+1)}{2} \\ \frac{(n+2)(n-1)}{2\times 2} & 0 & \cdots & 0 & 0 \\ 0 & \frac{(n+3)(n-2)}{2\times 3} & \cdots & 0 & 0 \\ \vdots & \vdots & \ddots & \vdots & \vdots \\ 0 & 0 & \cdots & 1 & 0 \end{bmatrix} \tag{48}$$

with coefficients,

$$A_n^{ij} = \begin{cases} \dfrac{-n(n+1)c}{2R} & \text{if } i = 1, \\ \dfrac{(n+i)(n-i+1)c}{2iR} & \text{if } i = j+1, \\ 0 & \text{otherwise.} \end{cases} \tag{49}$$

With scaling (36), every coefficient in the matrices $\boldsymbol{A}_n$ are scaled by a common factor of c/R. The non-homogenous vector function $\boldsymbol{\Phi}_{nm}$ has the nmth coefficient of ϕ on Γ as its only non-zero component

$$\boldsymbol{\Phi}_{nm}(t) = [c\phi_{nm}|_{r=R}, 0, \ldots, 0]^{\mathrm{T}}, \tag{50}$$

where

$$\phi_{nm}|_{r=R} = (\phi, Y_{nm})_\Gamma \equiv \int_0^{2\pi}\int_0^{\pi} Y_{nm}^*(\theta,\varphi)\phi(R,\theta,\varphi,t)\sin\theta\ \mathrm{d}\theta\ \mathrm{d}\varphi. \tag{51}$$

The scaling (37) used in Ref. [8] leads to a system of differential equations in the same form as Eq. (47) but with a different coefficient matrix $\tilde{\boldsymbol{A}}_n$

$$\tilde{A}_n^{ij} = \begin{cases} \dfrac{-n(n+1)c}{2R^j} & \text{if } i = 1, \\ \dfrac{(n+i)(n-i+1)c}{2i} & \text{if } i = j+1, \\ 0 & \text{otherwise.} \end{cases} \tag{52}$$

The first row of $\tilde{\boldsymbol{A}}_n$ is a function of $1/R^j$ for $j = 1, \ldots, n$. For large n and $R < 1$ this may lead to an ill-conditioned system.

The stability of a numerical solution to the system of differential (47) is determined by the eigenvalues of the coefficient matrix $\boldsymbol{A}_n$. If the real part of the eigenvalues are negative, the numerical solution will be asymptotically stable. Solutions to Eq. (47) are equivalent to solutions of the nth-order differential (32). As a result, the eigenvalues of matrices $\boldsymbol{A}_n$ are equivalent to the roots of the characteristic polynomial associated with Eq. (32), i.e.,

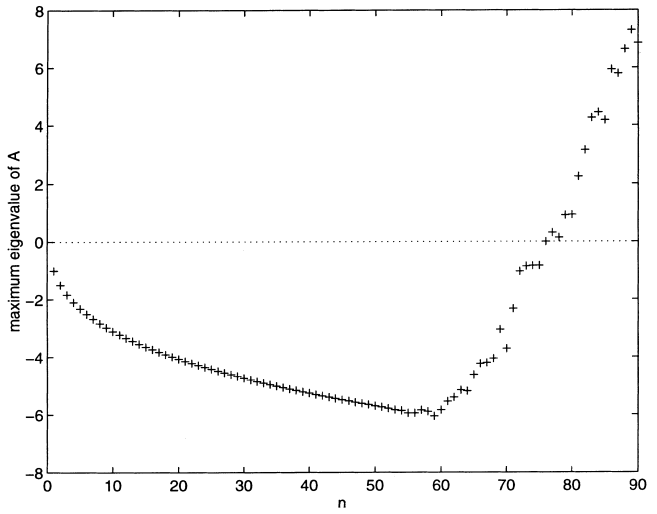

Fig. 1. Maximum real part of eigenvalues of coefficient matrix $\boldsymbol{A}_n$ normalized with c/R, vs. dimension n.

$$\det(\boldsymbol{A}_n - \lambda I) = \sum_{j=0}^{n} \frac{1}{c^{n-j}} \frac{a_n^j}{R^j} \lambda^{n-j} = 0. \tag{53}$$

The eigenvalues of the matrix $\boldsymbol{A}_n$ appearing in Eq. (47) are identical to the eigenvalues of $\tilde{\boldsymbol{A}}_n$ since they both are derived from the original nth-order differential Eq. (32). The eigenvectors associated with $\boldsymbol{A}_n$ and $\tilde{\boldsymbol{A}}_n$ will be different since they are based on a different scaling of $\boldsymbol{z}_{nm}$.

The eigenvalues λ may be normalized with the common factor c/R appearing in Eq. (48),

$$\tilde{\lambda} = \frac{R}{c}\lambda, \tag{54}$$

resulting in the polynomial

$$\sum_{j=0}^{n} a_n^j \tilde{\lambda}^{n-j} = 0. \tag{55}$$

The roots (eigenvalues) of Eq. (53) coincide with the roots of Eq. (55) multiplied by c/R.

In Ref. [9] it was verified numerically that the roots of Eq. (55) lie strictly in the left half of the complex plane up to $n = 76$. Fig. 1 shows numerical solutions for the maximum real part of the eigenvalues associated with matrix $\boldsymbol{A}_n$ normalized with c/R, i.e., $\max(\mathrm{Re}\,\tilde{\lambda})$ vs. dimension n. These results verify that the $\max(\mathrm{Re}\,\lambda)$ are negative for $n \leqslant 76$. Based on these results, the series in Eq. (40) should be truncated at $N \leqslant 76$ for the boundary condition to be stable.

3. Finite element implementation

Define standard inner products,

$$(\delta\phi, \phi)_\Omega := \int_\Omega \delta\phi\phi \, \mathrm{d}\Omega,$$

$$(\delta\phi, \phi)_\Gamma := \int_\Gamma \delta\phi\phi \, \mathrm{d}\Gamma.$$

The variational equation within Ω is obtained as usual by multiplying Eq. (2) with a weighting function $\delta\phi(x)$, and using the divergence theorem to obtain,

$$\frac{1}{c^2}\left(\delta\phi, \frac{\partial^2\phi}{\partial t^2}\right)_\Omega + (\nabla\delta\phi, \nabla\phi)_\Omega = \left(\delta\phi, \frac{\partial\phi}{\partial n}\right)_\Gamma + (\delta\phi, f)_\Omega. \tag{56}$$

For a spherical boundary, the normal derivative on Γ is equivalent to a radial derivative, i.e. $\partial\phi/\partial n = \partial\phi/\partial r$. The exact NRBC Eq. (40) may be implemented directly by replacing the radial derivative on Γ with the radial derivative appearing in the B_1 operator (26), with the result

$$\frac{1}{c^2}\left(\delta\phi, \frac{\partial^2\phi}{\partial t^2}\right)_\Omega + (\nabla\delta\phi, \nabla\phi)_\Omega + \frac{1}{c}\left(\delta\phi, \frac{\partial\phi}{\partial t}\right)_\Gamma + \frac{1}{R}(\delta\phi, \phi)_\Gamma = L(\delta\phi), \tag{57}$$

where

$$L(\delta\phi) = (\delta\phi, f)_\Omega - \frac{1}{R}\sum_{n=1}^{\infty}\sum_{m=-n}^{n} \boldsymbol{e}_n \cdot \boldsymbol{z}_{nm}(\delta\phi, Y_{nm})_\Gamma. \tag{58}$$

Using a standard Galerkin finite element approximation, results in the following second-order system of ordinary differential equations in time for the global solution vector $\boldsymbol{\phi}(t)$

$$\boldsymbol{M}\ddot{\boldsymbol{\phi}}(t) + \boldsymbol{C}\dot{\boldsymbol{\phi}}(t) + \boldsymbol{K}\boldsymbol{\phi}(t) = \boldsymbol{F}(t), \quad t > 0, \tag{59}$$

where

$$\boldsymbol{M} = \int_\Omega \frac{1}{c^2}\boldsymbol{N}^{\mathrm{T}}\boldsymbol{N}\ \mathrm{d}\Omega, \quad \boldsymbol{C} = \int_\Gamma \frac{1}{c}\boldsymbol{N}^{\mathrm{T}}\boldsymbol{N}\ \mathrm{d}\Gamma, \tag{60}$$

$$\boldsymbol{K} = \int_\Omega (\nabla\boldsymbol{N})^{\mathrm{T}}(\nabla\boldsymbol{N})\ \mathrm{d}\Omega + \int_\Gamma \frac{1}{R}\boldsymbol{N}^{\mathrm{T}}\boldsymbol{N}\ \mathrm{d}\Gamma, \tag{61}$$

$$\boldsymbol{F}(t) = \int_\Omega \boldsymbol{N}^{\mathrm{T}} f(x,t)\ \mathrm{d}\Omega - \frac{1}{R}\sum_{n=1}^{N}\sum_{m=-n}^{n} \boldsymbol{e}_n \cdot \boldsymbol{z}_{nm}(t)\int_\Gamma \boldsymbol{N}^{\mathrm{T}} Y_{nm}\ \mathrm{d}\Gamma \tag{62}$$

and $\boldsymbol{N}(x)$ is an array of basis functions with compact support associated with each node in a finite element mesh. The sum over n is truncated at a finite value N. For $N = 0$, the formulation reduces to the B_1 boundary condition. For $N \geqslant 1$, the NRBC is global over Γ, yet only requires inner products of spherical harmonics within the force vector $\boldsymbol{F}$. As a result, the NRBC is easy to implement and does not disturb the banded/sparse structure of the finite element matrix equations. In Eq. (62), the functions $\boldsymbol{z}_{nm} = \{z_{nm}^j\}$ are solutions to the system of first-order equations (47).

4. Time-integration

Several time-marching schemes are developed to integrate the second-order equations (59) concurrently with the first-order equations (47). In the first method, we adopt the Newmark family [11] to integrate Eq. (59). Let $\boldsymbol{d}^k = \boldsymbol{\phi}(t_k)$, $\boldsymbol{v}^k = \dot{\boldsymbol{\phi}}(t_k)$, $\boldsymbol{a}^k = \ddot{\boldsymbol{\phi}}(t_k)$, be the numerical solution and $\boldsymbol{F}^k = \boldsymbol{F}(t_k)$ the force at time-step $t_k = k\Delta t$, then the Newmark method in predictor/corrector form is [12]

predictors:

$$\tilde{\boldsymbol{d}}^{k+1} = \boldsymbol{d}^k + \Delta t\boldsymbol{v}^k + \frac{\Delta t^2}{2}(1-2\beta)\boldsymbol{a}^k, \tag{63}$$

$$\tilde{\boldsymbol{v}}^{k+1} = \boldsymbol{v}^k + (1-\gamma)\Delta t\boldsymbol{a}^k, \tag{64}$$

solve for $\boldsymbol{a}^{k+1}$

$$\left(\boldsymbol{M} + \gamma\Delta t\boldsymbol{C} + \beta\Delta t^2\boldsymbol{K}\right)\boldsymbol{a}^{k+1} = \boldsymbol{F}^{k+1} - \boldsymbol{C}\tilde{\boldsymbol{v}}^{k+1} - \boldsymbol{K}\tilde{\boldsymbol{d}}^{k+1}. \tag{65}$$

correctors:

$$\boldsymbol{d}^{k+1} = \tilde{\boldsymbol{d}}^{k+1} + \beta\Delta t^2\boldsymbol{a}^{k+1}, \tag{66}$$

$$\boldsymbol{v}^{k+1} = \tilde{\boldsymbol{v}}^{k+1} + \Gamma \Delta t \boldsymbol{a}^{k+1}. \tag{67}$$

Any of the members of the Newmark family may be used, including the second-order accurate $\gamma = 1/2$, and unconditionally stable trapezoidal rule ($\beta = 1/4$), and conditionally stable central difference method ($\beta = 0$). When solving using the explicit central difference method, equations (65) may be decoupled using standard diagonal mass $\boldsymbol{M}$, and damping matrices $\boldsymbol{C}$, e.g. using nodal quadrature, row-sum technique, or the HRZ lumping scheme [14].

The solution of Eq. (65) requires that the forcing term $\boldsymbol{F}^{k+1}$ be available at time-step t_{k+1}, i.e.,

$$\boldsymbol{F}^{k+1} = \int_{\Omega} \boldsymbol{N}^{\mathrm{T}} f(x, t_{k+1}) \, \mathrm{d}\Omega - \frac{1}{R} \sum_{n=1}^{N} \sum_{m=-n}^{n} \boldsymbol{e}_n \cdot \boldsymbol{z}_{nm}(t_{k+1}) \int_{\Gamma} \boldsymbol{N}^{\mathrm{T}} Y_{nm} \, \mathrm{d}\Gamma. \tag{68}$$

To compute $\boldsymbol{a}^{k+1}$, we need the values of $\boldsymbol{z}_{nm}(t)$ at $t = t_{k+1}$. The numerical solution $\boldsymbol{z}_{nm}^{k+1} = \boldsymbol{z}_{nm}(t_{k+1})$ to the first-order differential equation (47) is computed concurrently using an explicit time-integrator; for example the second-order accurate Adams–Bashforth algorithm [13]

$$\boldsymbol{z}_{nm}^{k+1} = \boldsymbol{z}_{nm}^{k} + \frac{\Delta t}{2} \left[3\left(\boldsymbol{A}_n \boldsymbol{z}_{nm}^{k} + \boldsymbol{\Phi}_{nm}^{k} \right) - \left(\boldsymbol{A}_n \boldsymbol{z}_{nm}^{k-1} + \boldsymbol{\Phi}_{nm}^{k-1} \right) \right]. \tag{69}$$

Note that Eq. (69) requires only the evaluation at $t = t_k$, the value at $t = t_{k-1}$ being known from the previous step. The stability condition imposed on Δt by the Adams–Bashforth method depends on the eigenvalues λ of the coefficient matrix $\boldsymbol{A}_n$, that is $-1 \leqslant \lambda \Delta t \leqslant 0$ with critical time-step

$$\Delta t < \Delta t_c = \frac{1}{|\min(\mathrm{Re}\ \lambda)|}. \tag{70}$$

As shown in Fig. (2), $|\min(\mathrm{Re}\ \lambda)|$ increases with dimension n. Therefore, for a fixed c/R, the critical time-step Δt_c decreases when more terms N are included in the NRBC.

The complete algorithm proceeds as follows:

(A1) : **Algorithm 1**

1. Set $\boldsymbol{z}_{nm}^{0} = \boldsymbol{z}_{nm}^{-1} = 0$ and initialize $\boldsymbol{d}^{0}$ and $\boldsymbol{v}^{0}$,
2. Calculate $\boldsymbol{a}^{0}$ from $\boldsymbol{M}\boldsymbol{a}^{0} = \boldsymbol{F}^{0} - \boldsymbol{C}\boldsymbol{v}^{0} - \boldsymbol{K}\boldsymbol{d}^{0}$,
   $\boldsymbol{d}^{-1} = \boldsymbol{d}^{0} - \Delta t \boldsymbol{v}^{0} + \frac{\Delta t^2}{2} \boldsymbol{a}^{0}$,
3. Compute $\boldsymbol{\Phi}_{nm}^{k}$ and $\boldsymbol{\Phi}_{nm}^{k-1}$ from Eq. (51) and
   Compute $\boldsymbol{z}_{nm}^{k+1}$ using Eq. (69) for $n = 1, \ldots, N$,

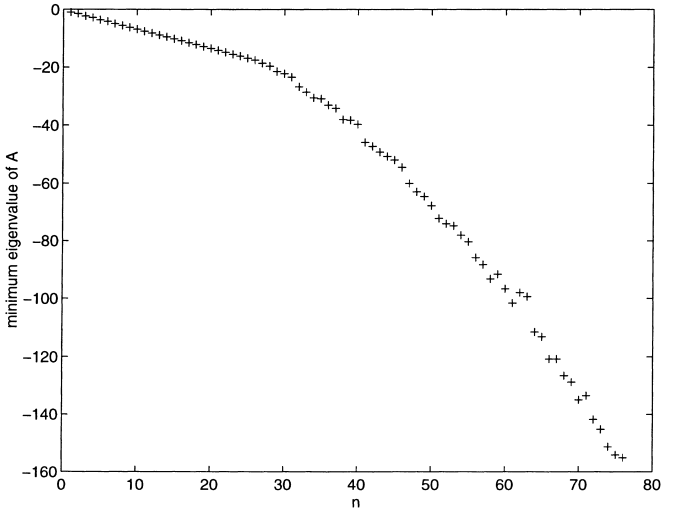

Fig. 2. Minimum real eigenvalues of matrix $\boldsymbol{A}_n$ scaled by c/R vs. dimension n.

4. Predict $\tilde{\boldsymbol{d}}^{k+1}$ and $\tilde{\boldsymbol{v}}^{k+1}$ from Eqs. (63) and (64),
   Calculate $\boldsymbol{a}^{k+1}$ from Eq. (65),
   Update $\boldsymbol{d}^{k+1}$ and $\boldsymbol{v}^{k+1}$ using Eqs. (66) and (67),
5. Increment k to $k+1$, Go back to Step 3.

In the above method, an explicit algorithm is used first to compute $\boldsymbol{z}_{nm}^{k+1}$ so that $\boldsymbol{F}^{k+1}$ is available to compute $\boldsymbol{d}^{k+1}$ from Eqs. (65) and (66).

We next show how to compute $\boldsymbol{d}^{k+1}$ and $\boldsymbol{z}_{nm}^{k+1}$ in parallel. In this algorithm, the central difference method [14] is applied directly to integrate Eq. (59)

$$\left(\frac{1}{\Delta t^2}\boldsymbol{M}+\frac{1}{2\Delta t}\boldsymbol{C}\right)\boldsymbol{d}^{k+1}=\boldsymbol{F}^{k}-\boldsymbol{K}\boldsymbol{d}^{k}+\frac{1}{\Delta t^2}\boldsymbol{M}\left(2\boldsymbol{d}^{k}-\boldsymbol{d}^{k-1}\right)+\frac{1}{2\Delta t}\boldsymbol{C}\boldsymbol{d}^{k-1}. \tag{71}$$

Eq. (71) is decoupled using standard diagonal mass and damping matrices. The solution of (71) requires only that the forcing term $\boldsymbol{F}^k$ be available. Therefore, to compute $\boldsymbol{d}^{k+1}$, we only need to evaluate values of $\boldsymbol{z}_{nm}(t)$ at $t=t_k$.

The solution $\boldsymbol{z}_{nm}^{k+1}$ to the ordinary differential equation (47) is advanced concurrently with $\boldsymbol{d}^{k+1}$ using the explicit Adams–Bashforth algorithm (69).

The complete algorithm proceeds as follows:

(A2) : Algorithm 2

1. Set $\boldsymbol{z}_{nm}^{0}=\boldsymbol{z}_{nm}^{-1}=0$ and initialize $\boldsymbol{d}^0$ and $\boldsymbol{v}^0$,
2. Calculate $\boldsymbol{a}^0$ from $\boldsymbol{M}\boldsymbol{a}^0=\boldsymbol{F}^0-\boldsymbol{C}\boldsymbol{v}^0-\boldsymbol{K}\boldsymbol{d}^0$,
   $\boldsymbol{d}^{-1}=\boldsymbol{d}^0-\Delta t\boldsymbol{v}^0+\frac{\Delta t^2}{2}\boldsymbol{a}^0$,
3. Compute $\boldsymbol{d}^{k+1}$ from Eq. (71),
4. Compute $\boldsymbol{\Phi}_{nm}^{k}$ and $\boldsymbol{\Phi}_{nm}^{k-1}$ from Eq. (51) and
   Calculate $\boldsymbol{z}_{nm}^{k+1}$ using Eq. (69) for $n=1,\ldots,N$,
5. Increment k to $k+1$, Go back to Step 3.

Steps 3 and 4 may be computed in parallel. The stability condition for central difference method with lumped mass is

$$\Delta t\leqslant\frac{h}{\sqrt{3}c}, \tag{72}$$

where Δt is the time-step, h is the smallest element size in a three-dimensional finite element mesh. Generally, for a given mesh and N, the stability constraint on Δt imposed by the explicit central difference method applied to Eq. (59) is more restrictive than the explicit Adams–Bashforth method Eq. (69) applied to Eq. (47).

Alternatively, the numerical solution $\boldsymbol{z}_{nm}^{k+1}$ to the ordinary differential equation (47) may be computed using the second-order Adams–Moulton method (trapezoidal rule)

$$\left(\boldsymbol{I}-\frac{\Delta t}{2}\boldsymbol{A}_n\right)\boldsymbol{z}_{nm}^{k+1}=\left(I+\frac{\Delta t}{2}\boldsymbol{A}_n\right)\boldsymbol{z}_{nm}^{k}+\frac{\Delta t}{2}\left(\boldsymbol{\phi}_{nm}^{k+1}+\boldsymbol{\phi}_{nm}^{k}\right). \tag{73}$$

The implicit trapezoidal rule applied to Eq. (47) is unconditionally stable for $N\leqslant 76$.

In this case the solution procedure is

(A3) : Algorithm 3

1. Set $\boldsymbol{z}_{nm}^{0}=0$, and initialize $\boldsymbol{d}^0$ and $\boldsymbol{v}^0$,
2. Calculate $\boldsymbol{a}^0$ from $\boldsymbol{M}\boldsymbol{a}^0=\boldsymbol{F}^0-\boldsymbol{C}\boldsymbol{v}^0-\boldsymbol{K}\boldsymbol{d}^0$,
   $\boldsymbol{d}^{-1}=\boldsymbol{d}^0-\Delta t\boldsymbol{v}^0+(\Delta t^2)/2\boldsymbol{a}^0$,
3. Compute $\boldsymbol{d}_{k+1}$ from Eq. (71),
4. Compute $\boldsymbol{\Phi}_{nm}^{k+1}$ and $\boldsymbol{\Phi}_{nm}^{k}$ from Eq. (51),
5. Compute $\boldsymbol{z}_{nm}^{k+1}$ from Eq. (73) for $n=1,\ldots,N$,
6. Increment k to $k+1$, Go back to Step 2.

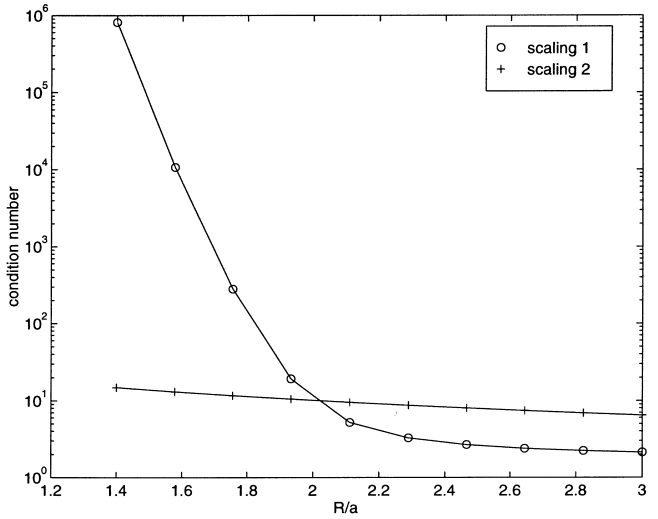

Fig. 3. Condition number of matrix $(\boldsymbol{I} - (\Delta t/2)\boldsymbol{A}_n)$ appearing in implicit Adams–Moulton method measured in L_2 norm vs. normalized truncation radius R/a. Comparison of definition $\boldsymbol{A}_n$, denoted Scaling 2, and definition $\tilde{\boldsymbol{A}}_n$, denoted Scaling 1.

The computational work required to solve the coupled linear systems (73) is negligible, because the matrices $\boldsymbol{A}_n$ are small. To ensure accurate solutions to Eq. (73) we examine the condition number of the matrix

$$\boldsymbol{D}_n := \left(\boldsymbol{I} - \frac{\Delta t}{2}\boldsymbol{A}_n\right),$$

denoted $\mathrm{cond}\,(\boldsymbol{D}_n)$, resulting from the Adams–Moulton method. If the condition number is close to 1, then small relative changes in the data can lead to only small relative changes in the solution, so that the problem is well-conditioned. If the condition number is large, the problem may become ill-conditioned, but not necessarily.

Consider the model problem of scattering from a sphere of radius $a = 0.5$. Assume an element mesh size of $h = \pi a/100$, with a time-step $\Delta t = h/\sqrt{3}c$, and take $N = 20$ terms in the series present in the NRBC. The $\mathrm{cond}(\boldsymbol{D}_n)$ for this problem measured in the L_2 matrix norm is plotted in Fig. 3 as a function of the non-reflecting boundary radius R. The condition number is given for $\boldsymbol{A}_n$ defined by Eqs. (49) and (52). Using scaling (36) to define $\boldsymbol{A}_n$ results in a condition number of approximately 10 which is relatively uniform as R decreases. In contrast, the scaling (37) results in a condition number which increases substantially for $R/a \leqslant 1.8$.

5. Numerical examples

Numerical experiments are performed to assess the accuracy and convergence properties of the NRBC when implemented in the finite element method. Comparisons are made to a local second-order boundary condition [2,3] and [4], denoted B_2

$$B_2\phi = \left(\frac{\partial}{\partial r} + \frac{r}{c}\frac{\partial^2}{\partial r \partial t} + \frac{r}{c^2}\frac{\partial^2}{\partial t^2} + \frac{2}{c}\frac{\partial}{\partial t} + \frac{1}{r} - \frac{1}{2r}\Delta_\Gamma\right)\phi = 0 \quad \text{on } \Gamma \tag{74}$$

with Laplace–Beltrami operator Δ_Γ defined as,

$$\Delta_\Gamma\phi := \frac{1}{\sin\varphi}\frac{\partial}{\partial\varphi}\left(\sin\varphi\frac{\partial\phi}{\partial\varphi}\right) + \frac{1}{\sin^2\varphi}\frac{\partial^2\phi}{\partial\theta^2}. \tag{75}$$

When B_2 is applied to the multiple expansion (29), then

$$B_2\phi = \mathrm{O}\left(\frac{1}{r^5}\right) \tag{76}$$

which shows that the boundary condition $B_2\phi = 0$ is more accurate than B_1.

We denote Eq. (40) by NR1(N), where N defines the number of harmonics included in the truncated series. NR1(0) annihilates the first harmonic appearing in Eq. (6) and coincides with the local boundary condition B_1 defined in Eqs. (1) and (25). Both NR1(1) and B_2 annihilate the first and second harmonics in Eq. (6). Two model problems are studied, in the first we investigate the ability of NR1(N) to annihilate high-order spherical harmonics on Γ, in the second we investigate the accuracy of NR1(N) for a challenging test problem of radiation from a piston on a sphere.

5.1. Spherical harmonic radiation

Consider time-dependent radiation from a sphere of radius $a = 1$, such that

$$\phi(a, \theta, t) = P_n(\cos\theta)\sin\omega t, \quad 0 \leqslant \theta \leqslant \pi, \quad t \geqslant 0. \tag{77}$$

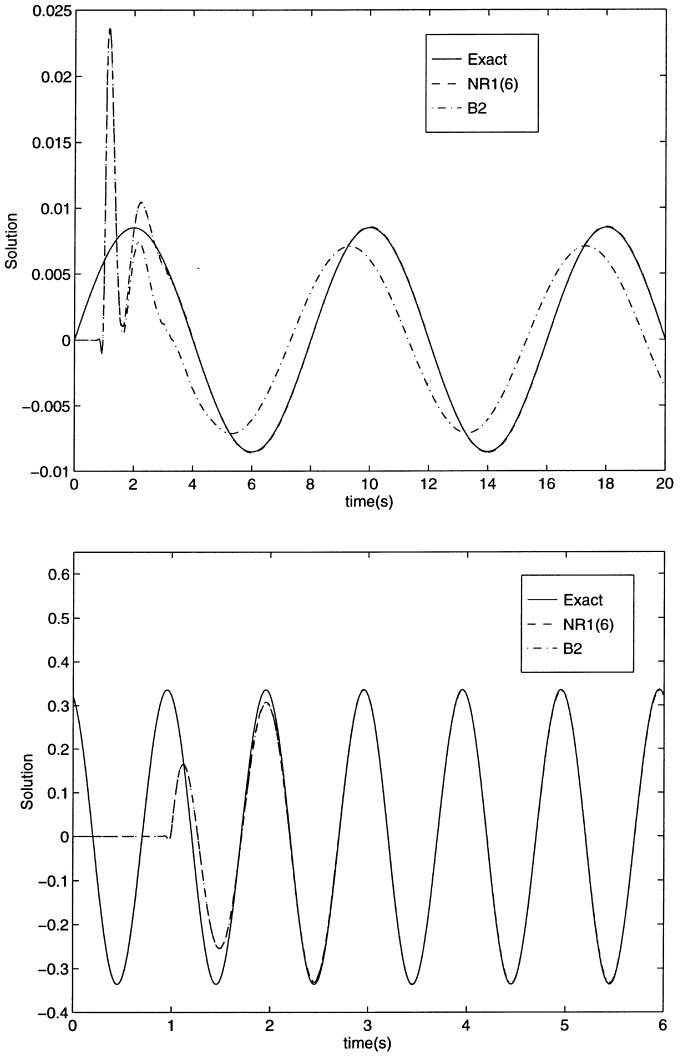

Fig. 4. Spherical wave harmonic $n = 6$. Time-dependent solutions computed using the boundary conditions B_2, and NR1(6) compared to the steady-state exact solution on Γ at $\theta = 0°$. (Top) Normalized frequency $\omega a/c = \pi/4$, mesh 20×120. (Bottom) Normalized frequency $\omega a/c = 2\pi$, mesh 40×240.

The exact steady-state solution for this problem is,

$$\phi(r,\theta,t) = -\mathrm{Imag}\left\{ \frac{h_n(kr)}{h_n(ka)} P_n(\cos\theta) \mathrm{e}^{-\mathrm{i}\omega t} \right\}, \quad r \geqslant a. \tag{78}$$

In the above, P_n are Legendre polynomials, h_n are spherical Hankel functions of the first kind, and $k = \omega/c$ is the wavenumber. The local boundary condition $B_1 = \mathrm{NR1}(0)$ annihilates the leading $1/r$ term in the multiple expansion (29) and is exact for the 'breathing' mode corresponding to $n = 0$ in Eqs. (77) and (78), yet only approximates higher modes. The local boundary condition B_2 annihilates the terms $1/r$ and $1/r^2$ in the expansion Eq. (29) and is exact for the first two modes corresponding to $n = 0$ and $n = 1$. The boundary condition NR1(N) annihilates the leading term $1/r$ in the expansion (29) and is exact for harmonics $n \leqslant N$.

The problem is axisymmetric and independent of φ. Therefore it is sufficient to compute the solution in the domain Ω defined by the (r,θ) plane for $a \leqslant r \leqslant R$, and $0 \leqslant \theta \leqslant \pi$. The artificial boundary Γ is located at $R = 2$. The computational domain is discretized with uniform meshes of standard 4-node bilinear axisymmetric finite elements.

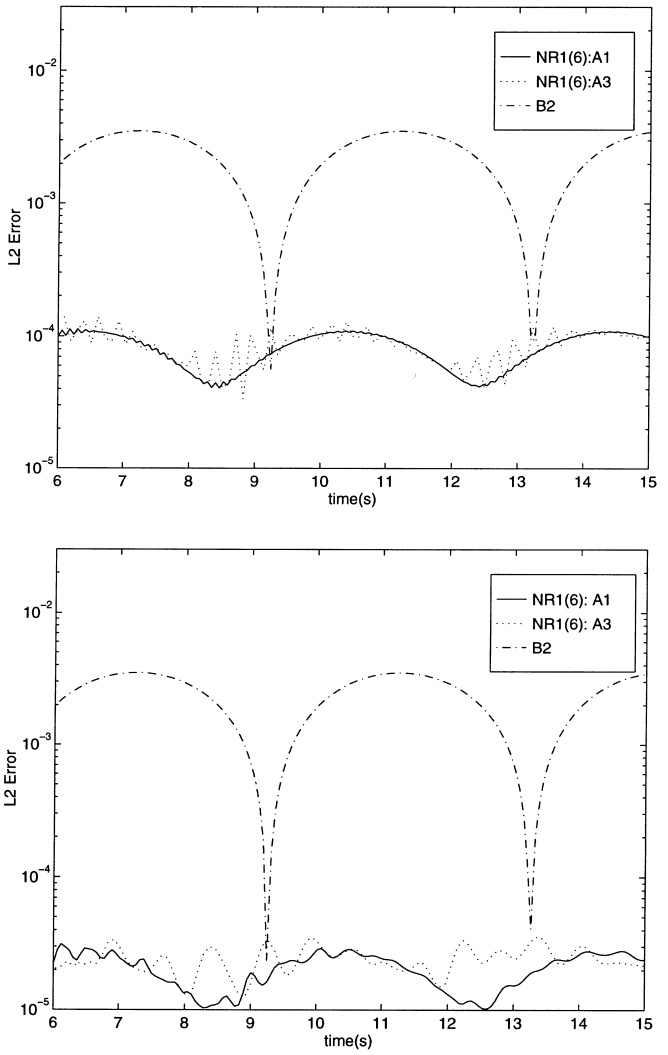

Fig. 5. Spherical wave harmonic $n = 6$. Time-dependent solutions computed using the boundary conditions B_2, and NRI (6) compared to the steady-state exact solution on Γ at $\theta = 0°$. (Top) Normalized frequency $\omega a/c = \pi/4$, mesh 20×120. (Bottom) Normalized frequency $\omega a/c = 2\pi$, mesh 40×240.

We begin with a calculation driven with $n = 6$ and a relatively low frequency $\omega a/c = \pi/4$ on a mesh with 20×120 elements (20 evenly spaced elements in $1 \leqslant r \leqslant 2$, and 120 evenly spaced elements in $0 \leqslant \theta \leqslant \pi$). A time-harmonic solution is obtained by starting from rest with initial data ϕ_0 and $\dot{\phi}_0$ equal to zero and driving the solution to steady-state with a time-step $\Delta t = 0.03$. Numerical results using NR1(N) are obtained using both (A1): Algorithm 1, and (A3): Algorithm 3.

Fig. 4 (Top) shows time-dependent solutions at the pole of Γ, $R = 2$, and $\theta = 0$, obtained using B_2, NR1(6), and the exact steady-state solution. The numerical solution using B_2 exhibits both large amplitude and phase errors. The solution obtained using NR1(6) can barely be distinguished from the exact time-harmonic solution in the steady-state interval beyond $t > 6$. The instantaneous error $e(t) = \phi^h - \phi$, measured in L_2 norm on Γ is defined as,

$$E(t) = \left\{ \int_\Gamma \left[\phi^h(R,\theta,t) - \phi(R,\theta,t)\right]^2 \mathrm{d}\Gamma \right\}^{1/2}, \tag{79}$$

where ϕ^h is the approximate finite element solution and ϕ is the exact steady-state solution. The error $E(t)$ is shown in Fig. 5 (Top) over the steady-state interval $6 \leqslant t \leqslant 15$. By using NR1(6) instead of B_2, the error is

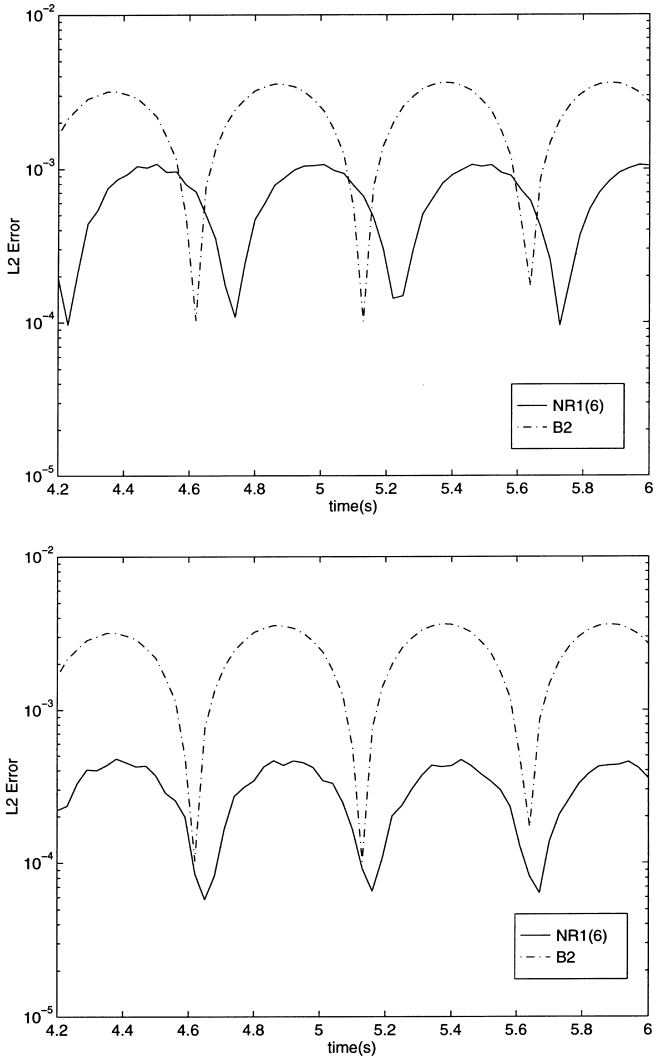

Fig. 6. Spherical wave harmonic $n = 6$, and normalized frequency $\omega a/c = \pi/4$. The L_2 error $E(t)$ on Γ for the boundary conditions B_2, and NR1(6), computed using (A1): Algorithm 1, and (A3): Algorithm 3. (Top) Mesh: 20×120. (Bottom) Mesh: 40×240.

reduced by an order of magnitude in accuracy. The solution using Algorithm 3 shows some small-amplitude oscillation in the numerical solution.

In Fig. 5 (Bottom) we perform the same comparison with a mesh refined by a factor of two in r and θ, i.e. 40×240 elements. Using this refinement, the error drops by a factor of nearly four, indicating second-order convergence to the exact solution, and the error in using NR1(6) is due to discretization error only. The solution obtained using B_2 does not improve significantly with the refined mesh, indicating that the error using B_2 is dominated by spurious reflection.

In Fig. 4 (Bottom) and Fig. 6, we perform the same comparison with the frequency increased to $\omega a/c = 2\pi$ on the 40×240 mesh. To minimize time-integration error, we decrease the time-step to $\Delta t = 0.01$. Fig. 4 (Bottom) shows the time-dependent solution at the pole, $R = 2$, and $\theta = 0$. The error $E(t)$ is shown in Fig. 6. The maximum error due to B_2 is slightly less than 4% and is smaller than the lower frequency case. This is expected since the accuracy of solutions obtained from local boundary conditions tend to increase with an increase in wavenumber [4]. By using NR1(6) instead of B_2, the error is reduced by a factor of four to 1%. Fig. 6 (Bottom), shows the error for a refined mesh using 60×240 elements. The

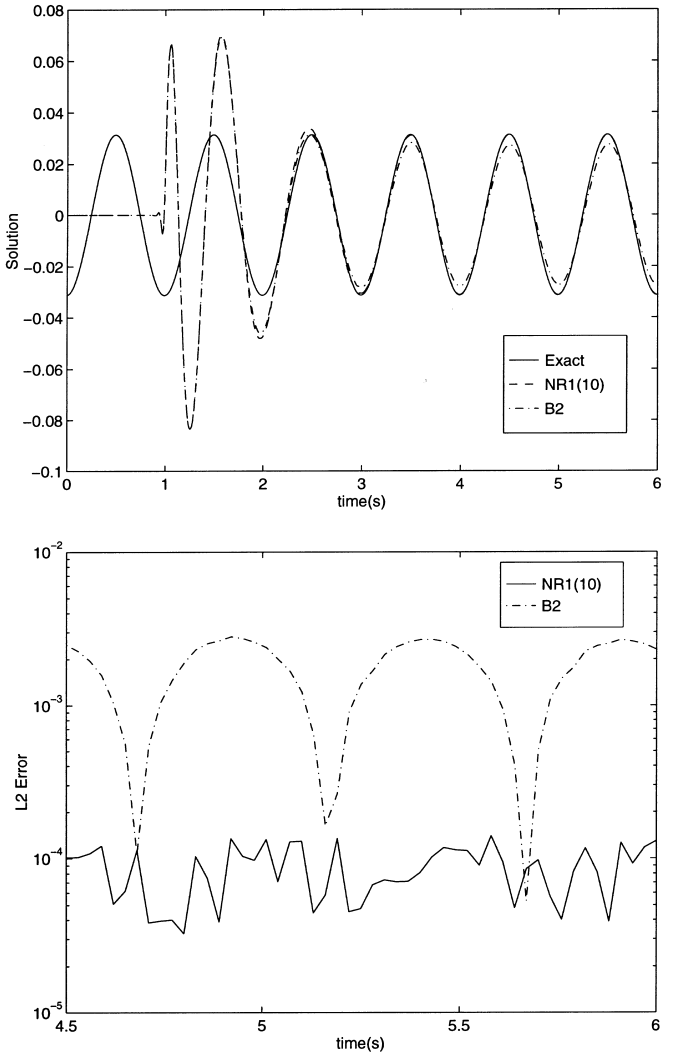

Fig. 7. Spherical wave harmonic $n = 10$, and normalized frequency $\omega a/c = 2\pi$. Mesh: 60×360. (Top): Time-dependent solutions computed using the boundary conditions B_2, and NR1(10) compared to the steady-state exact solution on Γ at $\theta = 0°$. (Bottom): The L_2 error $E(t)$ on Γ.

refined mesh reduces the discretization error in the NR1(6) solution by a factor of two to less than 0.5%, while the B_2 solution does not improve.

As the harmonic driver is increased to $n = 10$, the acoustic radiation pattern becomes more complex. Fig. 7 (Top), shows the time-dependent solution at the pole computed on a 60×360 mesh and driving frequency of $\omega a/c = 2\pi$. The error $E(t)$ is shown in Fig. 7 (Bottom). The solution using B_2 exhibits relatively large amplitude and phase errors. This result demonstrates the difficulty low-order boundary conditions have when attempting to absorb high-order harmonics on Γ. In contrast, the solution using NR1(10) can barely be distinguished from the exact time-harmonic solution in the steady-state interval. By using NR1(10) instead of B_2, the error is reduced by over an order of magnitude in accuracy.

5.2. Radiation from a piston on a sphere

To study the accuracy of the NRBC for a problem involving an infinite number of spherical harmonics, we consider axisymmetric radiation from a circular piston on a sphere with radius $a = 0.5$, see [4,16]. The piston is represented by time-harmonic motion $\phi(a,\theta,t) = \sin\omega t$ in the range $0^\circ \leqslant \theta \leqslant 15^\circ$, and $\phi(a,\theta,t) = (30^\circ - \theta)\sin\omega t/15^\circ$ over $15^\circ \leqslant \theta \leqslant 30^\circ$, and $\phi(a,\theta,t) = 0$ otherwise. This problem is challenging because the waves radiated at the piston pole $\theta = 0^\circ$ are attenuated as they travel along longitudes down to the south pole $\theta = 180^\circ$. In the region opposite the piston, the amplitude of the waves are significantly lower than near the piston.

We use a 20×120 mesh of axisymmetric elements (20 in $0.5 \leqslant r \leqslant 1.0$ and 120 in $0 \leqslant \theta \leqslant 180^\circ$), with a driving frequency set at $\omega a/c = \pi$. Results are compared to the second-order local boundary condition (74), denoted B_2, and a finite element solution obtained from a large mesh which extends beyond the region influenced by the transient disturbance, denoted IM. For a spherical truncation boundary set at $R = 1.0$ and $N \leqslant 20$, the minimum eigenvalue (real part) of the system matrix $\boldsymbol{A}_n$ is $\lambda_{min} = -13.57$. For the Adams–Bashforth algorithm, this results in a stability condition $\Delta t < 0.074$. We use a time-step $\Delta t = 0.01$, and compare solutions for NR1(N) using Algorithms 1 and 3.

Fig. 8 (Top) compares contours of finite element solutions obtained using B_2, NR1(20), and the infinite mesh solution, IM, at time $t = 4$. The solution sample time is chosen such that steady-state has been reached and several spurious reflections between Γ and the radiating sphere could have occurred. The solution obtained using B_2 captures the physics of the solution in the vicinity of the piston yet shows a

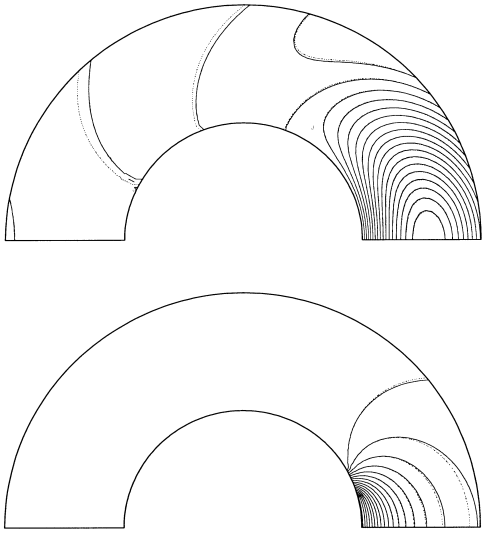

Fig. 8. Solution contours for radiating piston on a sphere. Solid contour lines denote infinite mesh solution (IM); Dashed contours denote NR1(20); Dotted contours denote B_2. (Top) Normalized frequency $\omega a/c = \pi$, at $t = 4$, (Bottom) Normalized frequency $\omega a/c = \pi/8$, at $t = 10.5$.

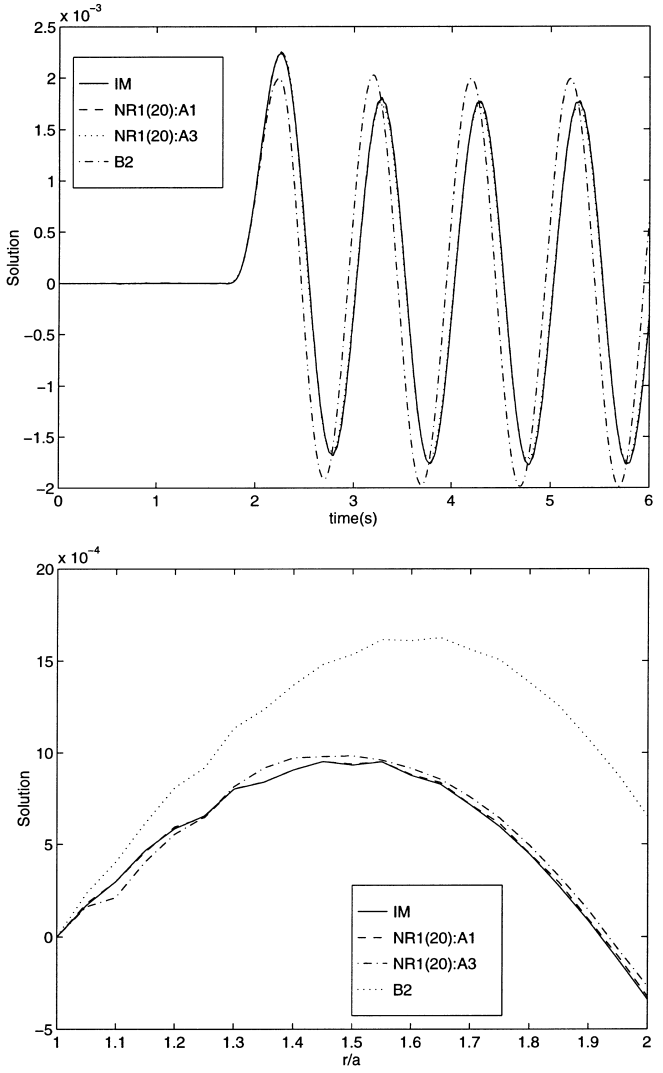

Fig. 9. Radiation from a piston on a sphere of radius $a = 0.5$ and normalized frequency $\omega a/c = \pi$. (Top) Time-dependent solutions computed for B_2, and NR1(20), computed using Algorithms A1 and A3, compared to infinite mesh (IM) solution at $R = 1.0$, and $\theta = 180°$. (Bottom) Solution profile for $\theta = 180°$, and $0.5 \leqslant r \leqslant 1.0$, at $t = 6$.

Table 1
Radiation from piston at $ka = \pi$. Comparison of max (L_2 error) ($\times 10^{-4}$) at $r/a = 1.5$ for NR1(N), $0 \leqslant N \leqslant 20$ and B_2, and truncation boundary radius $R/a = 1.5 \leqslant R \leqslant 2.5$

NR1	Boundary radius R/a			
N	1.5	1.75	2.0	2.5
0	226.19	119.30	84.95	56.11
3	191.01	87.73	55.90	39.58
5	61.32	15.63	6.23	2.18
6	24.34	4.35	1.64	1.25
7	7.55	1.27	1.04	1.24
10	2.38	1.21	1.03	1.24
15	1.25	1.21	1.03	1.24
20	1.25	1.21	1.03	1.24
B_2	54.24	18.43	8.82	3.38

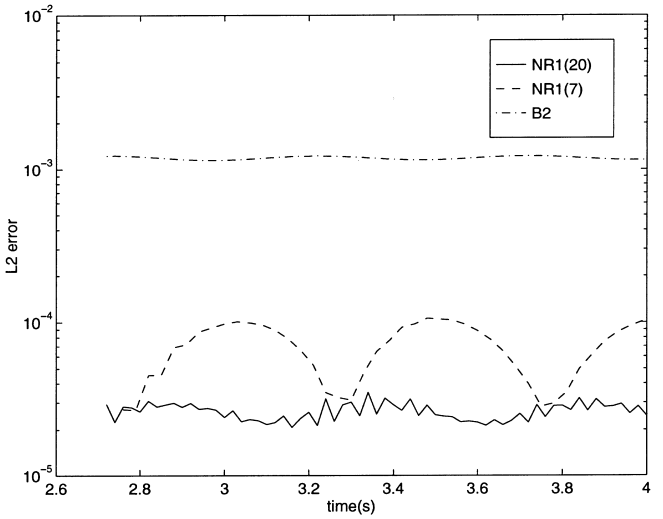

Fig. 10. Instantaneous error $E(t)$ on the truncation boundary $R = 1.0$ due to a radiating piston on a sphere of radius $a = 0.5$ and normalized frequency $\omega a/c = \pi$. Results compared for boundary condition B_2, and NR1(N) using $N = 7$ and $N = 20$ terms in the truncated series.

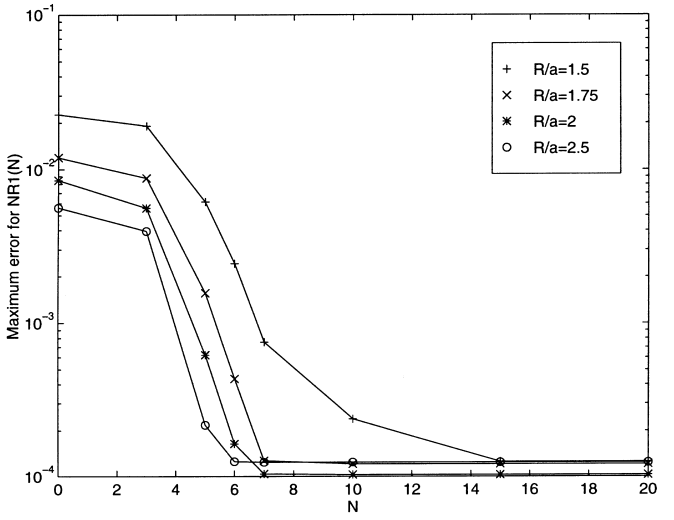

Fig. 11. Radiation from a piston on a sphere of radius $a = 0.5$ and normalized frequency $\omega a/c = \pi$. The maximum error measured at $r = 0.75$ for the NR1(N) solution as a function of the number of terms N included in the NRBC. Results plotted for the artificial boundary Γ positioned at $R = 0.75$ to $R = 1.25$.

significant loss in accuracy in the more difficult south pole region $\theta = 180°$. In contrast, the contour lines for the NR1(20) matches the infinite solution throughout the computational domain.

In Fig. 9 (Top), these observations are quantified by plotting time-dependent solutions at the south pole of Γ, $r = R$ and $\theta = 180°$. In Fig. 9 (Bottom) the solution profile is displayed at time $t = 6$ along the z-axis, $0.5 \leqslant r \leqslant 1$ and $\theta = 180°$. The solution using B_2 shows significant spurious reflection at the south pole, while NR1(20) coincides almost perfectly with the IM solution. Fig. 10 shows the instantaneous error $E(t)$ at $R = 1.0$ measured in L_2 norm after the solution has reached steady-state. The results illustrate the reduction in error obtained from increasing the number of terms in the truncated series from $N = 7$ to $N = 20$.

In Fig. 11 and Table 1, we compare the maximum error at steady-state obtained using NR1(N), for N increasing from 0 to 20. Results are given at $r = 0.75$ for four different computational domains positioned with truncation boundary at $R/a = 1.5, 1.75, 2.0, 2.5$ respectively. These results show the interplay between

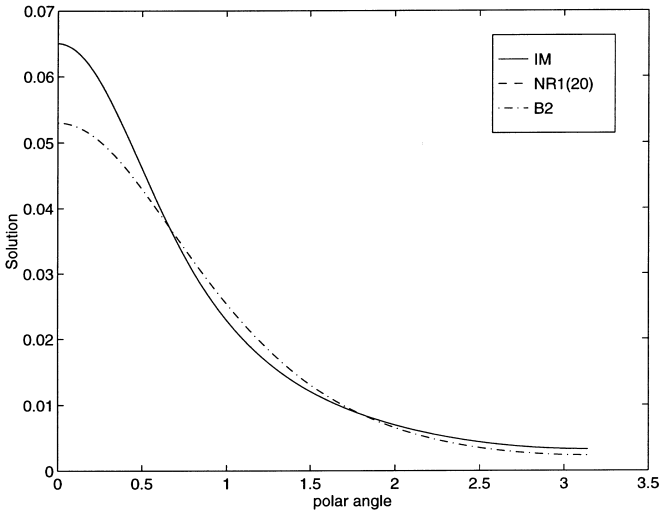

Fig. 12. Solution profile on the truncation boundary Γ, $r = R$ and $0 \leqslant \theta \leqslant \pi$, at $\omega a/c = \pi/8$, and $t = 11.5$ for a piston on a sphere.

Table 2
Comparison of max (L_2 error) during steady-state for normalized frequencies $ka = \pi$, and $ka = \pi/8$

ka	B_2	NR1(20)
π	1.2317×10^{-3}	3.4911×10^{-5}
$\pi/8$	3.1993×10^{-3}	1.0365×10^{-5}

the number of terms N used in NR1(N) and the approximation to harmonic modes for $n > N$. Recall that NR1(0) coincides with the local B_1 boundary condition. NR1(N) is exact for all modes $n \leqslant N$. For harmonic modes $n > N$, NR1 approximates the solution by annihilating the leading term $1/r$. B_2 approximates high-order modes by annihilating leading terms $1/r$ and $1/r^2$ for all modes, and thus will be more accurate than NR1(N) when only a few terms N are included. For this problem, we observe that the B_2 boundary condition is more accurate than NR1(N) for $N < 5$. For $N > 5$ the error is reduced by an order of magnitude and is significantly lower than the error using B_2. As N is increased the solution converges to a finite error value of approximately 1×10^{-4}. This limiting value is controlled primarily by the boundary approximation of the term $(\boldsymbol{N}, Y_{nm})_\Gamma$ appearing in Eq. (62).

As the truncation boundary radius R is reduced, more terms N are required to accurately represent the solution. In particular, when the radius is reduced to $R/a = 1.5$, $N = 15$ terms are needed for the error to converge, whereas when $R/a = 2.0$, only $N = 7$ terms are needed. For B_2 to approach the accuracy of the NRBC NR1(15) at $R/a = 1.5$, the truncation radius must be larger than $R/a = 2.5$. This triples the size of the computational domain, which triples both memory requirements and total execution time. For NR1(15) the extra computer time to compute the inner products (ϕ, Y_{nm}) over Γ and advance the functions $\boldsymbol{z}_{nm}(t)$ for $|m| \leqslant n, 1 \leqslant n \leqslant 15$ is small. The additional memory needed to store the functions $\boldsymbol{z}_{nm}(t)$ is only of the order of $\sim N^3$ scalar values, independent of the mesh size used in Ω. This extra storage is negligible compared to the memory required to solve the finite element equations, especially on a three-dimensional mesh. In practice, it is not usually necessary to use more than $N = 25$ terms to obtain good accuracy.

We finally compare the effect of decreasing the frequency using the local boundary condition B_2, with that of NR1(20). Fig. 8 (Bottom) compares contours of finite element solutions obtained using B_2, NR1(20), and the infinite mesh solution, IM, at a reduced frequency $ka = \pi/8$. Fig. 12 shows the solution profile on Γ. The solution obtained using B_2 shows significant error, even in the vicinity of the piston. In contrast, NR1(20) matches the infinite solution throughout Ω. Table 2 gives the maximum error measured

in L_2 norm on Γ for a fixed value of $N = 20$ and $R/a = 2$. The accuracy of the boundary condition NR1 improves as the frequency is reduced from $ka = \pi$, to $ka = \pi/8$, because the solution becomes smoother. In contrast, the accuracy of B_2 tends to deteriorate as the frequency is lowered, as expected [4].

6. Conclusions

In conclusion, the NRBC have been found to be very accurate in finite element computations, are easy to implement and require little extra memory. We have shown that their derivation follows directly from a recurrence result given by Lamb [10]. An alternate scaling of the boundary variables lead to a well-conditioned coefficient matrix. Three algorithms were presented to numerically solve the semidiscrete finite element equations combined with the NRBC. In the first algorithm, we use standard time-marching schemes from the Newmark family implemented in predictor/corrector form, to integrate the finite element equations, while the solution to the first-order boundary equations are computed concurrently using the explicit Adams–Bashforth method. In the second algorithm, we use the explicit central difference method to integrate the finite element equations combined with the explicit Adams–Bashforth method for the boundary equations. In the third method, we use the explicit central difference method for finite element equations, and the implicit Adams–Moulton (trapezoidal rule) for the boundary equations. All three algorithms are multi-step methods that are easy to implement in standard finite element codes. Other closely related multi-step methods, such as the HHT-α method [17] can also be used to advance the solution in time with no significant changes to the time-marching schemes presented. Although the boundary conditions are global over the truncation boundary, when implemented in the finite element method, they only require inner products of spherical harmonics (ϕ, Y_{nm}) over Γ, appearing in the force vector, and as a result, they are easy to implement and do not disturb the banded/sparse structure of the matrix equations. The extra computer time and memory required to evaluate the inner products (ϕ, Y_{nm}) over Γ and advance the boundary functions $z_{nm}(t)$ is negligible compared to the memory and time required to solve the finite element equations, especially on a three-dimensional mesh. In practice, it is not usually necessary to use more than $N = 25$ terms to obtain good accuracy.

Numerical studies confirm the ability of the NRBC to annihilate spherical harmonics on the truncation boundary. Results show significant improvement in accuracy over the local B_2 operator, especially as the truncation boundary is positioned near the source of scattering/radiation and for low frequencies. For a given level of accuracy, the NRBC give a large reduction in computer memory and execution time compared to the B_2 boundary condition.

Acknowledgements

Support for this work was provided by the National Science Foundation under Grant CMS-9702082 in conjuction with a Presidential Early Career Award for Scientists and Engineers (PECASE), and is gratefully acknowledged.

Appendix A

Expanding Eq. (16) leads to an operator form involving nth-order radial derivatives. The kth term takes the form,

$$\phi_k = \prod_{j=1}^{k} \left(\frac{\partial}{\partial r} - \frac{j-1}{r} \right) \frac{v_k(r-ct)}{r} = \sum_{j=0}^{k} \frac{(-1)^j}{r^{j+1}} a_k^j \frac{\partial^{k-j}}{\partial r^{k-j}} v_k(r-ct), \tag{A.1}$$

where a_k^j are coefficients to be determined. To obtain evolution formula for a_k^j, we develop an expression for ϕ_{k+1},

$$\phi_{k+1} = \prod_{j=1}^{k+1}\left(\frac{\partial}{\partial r} - \frac{j-1}{r}\right)\frac{v_{k+1}(r-ct)}{r} = \left(\frac{\partial}{\partial r} - \frac{k}{r}\right)\prod_{j=1}^{k}\left(\frac{\partial}{\partial r} - \frac{i-1}{r}\right)\frac{v_{k+1}(r-ct)}{r}. \tag{A.2}$$

Expanding,

$$\begin{aligned}\phi_{k+1} &= \left(\frac{\partial}{\partial r} - \frac{k}{r}\right)\left[\sum_{j=0}^{k}\frac{(-1)^j}{r^{j+1}}a_k^j\frac{\partial^{k-j}}{\partial r^{k-j}}v_{k+1}(r-ct)\right] \\ &= \sum_{j=0}^{k}\frac{(-1)^{j+1}}{r^{j+2}}(k+j+1)a_k^j\frac{\partial^{k-j}}{\partial r^{k-j}}v_{k+1} + \sum_{j=0}^{k}\frac{(-1)^j}{r^{j+1}}a_k^j\frac{\partial^{k+1-j}}{\partial r^{k+1-j}}v_{k+1}\end{aligned} \tag{A.3}$$

and collecting terms we have,

$$\phi_{k+1} = \frac{a_k^0}{r}\frac{\partial^{k+1}}{\partial r^{k+1}}v_{k+1} + \sum_{j=1}^{k}\frac{(-1)^j}{r^{j+1}}\left[a_k^j + (k+j)a_k^{j-1}\right]\frac{\partial^{k+1-j}}{\partial r^{k+1-j}}v_{k+1} + \frac{(-1)^{k+1}}{r^{k+2}}(2k+1)a_k^k v_{k+1}. \tag{A.4}$$

Equating coefficients in Eq. (A.4) with coefficients in Eq. (A.1) for k replaced by $k+1$, we obtain the evolution equation for a_k^j,

$$a_{k+1}^0 = a_k^0, \tag{A.5}$$

$$a_{k+1}^j = a_k^j + (k+j)a_k^{j-1}, \quad 1 \leqslant j \leqslant k, \tag{A.6}$$

$$a_{k+1}^{k+1} = (2k+1)a_k^k. \tag{A.7}$$

From Eq. (17) we have the starting values,

$$a_1^0 = 1, \qquad a_1^1 = 1. \tag{A.8}$$

From Eq. (A.5) and $a_1^0 = 1$, we obtain the coefficients for $j = 0$,

$$a_n^0 = 1. \tag{A.9}$$

From recursive use of Eq. (A.7) and $a_1^1 = 1$, we obtain the coefficient for $j = n$,

$$a_n^n = (2n-1)a_{n-1}^{n-1} = (2n-1)(2n-3)\cdots(5)(3)(1) = \frac{(n+n)!}{2^n n!}. \tag{A.10}$$

The coefficients for $1 \leqslant j \leqslant n-1$ are obtained from Eq. (A.6). In the following, we make use of the result,

$$\sum_{k=j}^{n-1}\left(a_{k+1}^j - a_k^j\right) = a_n^j - a_j^j, \qquad j = 1, \ldots, n-1. \tag{A.11}$$

From Eqs. (A.6) and (A.11), we have,

$$a_n^j = a_j^j + \sum_{k=j}^{n-1}(k+j)a_k^{j-1}. \tag{A.12}$$

For $j = 1$ and using the starting value $a_1^1 = 1$,

$$a_n^1 = \sum_{k=0}^{n-1}(k+1) = \frac{(n+1)!}{2(n-1)!}. \tag{A.13}$$

For $j = 2$,

$$a_n^2 = a_2^2 + \sum_{k=2}^{n-1}(k+2)a_k^1. \tag{A.14}$$

Using Eqs. (A.13) and (A.10), we have

$$a_n^2 = \sum_{k=1}^{n-1}\frac{(k+2)(k+1)k}{2} = \frac{(n+2)!}{2^2 2!(n-2)!}. \tag{A.15}$$

For $j = 3$, and using Eqs. (A.10) and (A.15),

$$a_n^3 = \sum_{k=2}^{n-1}\frac{(k+3)(k+2)(k+1)k(k-1)}{2^2 2!} = \frac{(n+3)!}{2^3 3!(n-3)!}. \tag{A.16}$$

By induction,

$$a_k^j = \frac{(k+j)!}{2^j j!(k-j)!}. \tag{A.17}$$

so that

$$a_n^j = a_j^j + \sum_{k=j}^{n-1}(k+j)a_k^{j-1} = \sum_{k=j-1}^{n-1}\frac{(k+j)!}{2^{j-1}(j-1)!(k-j+1)!} = \frac{(n+j)!}{2^j j!(n-j)!}. \tag{A.18}$$

References

[1] D. Givoli, Numerical methods for problems in infinite domains, in: Studies in Applied Mechanics, vol. 33, Elsevier, Amsterdam, 1992.
[2] A. Bayliss, E. Turkel, Radiation boundary conditions for wave-like equations, Commun. Pure Appl. Math. 33 (1980) 707–725.
[3] P.M. Pinsky, N.N. Abboud, Finite element solution of the transient exterior structural acoustics problem based on the use of radially asymptotic boundary operators, Comput. Meth. Appl. Mech. Engrg. 85 (1991) 311–348.
[4] L.L. Thompson, P.M. Pinsky, A space-time finite element method for structural acoustics in infinite domains Part 2: Exact time-dependent NRBC, Comput. Meth. Appl. Mech. Engrg. 132 (1996) 229–258.
[5] J.B. Keller, D. Givoli, Exact NRBC, J. Comp. Phys. 82 (1989) 172–192.
[6] L.W. Pearson, R.A. Whitaker, L.J. Bahrmasel, An exact radiation boundary condition for the finite-element solution of electromagnetic scattering on an open domain, IEEE Trans. Magnetics 25 (4) (1989) 3046–3048.
[7] L.L. Thompson and P.M. Pinsky, New space-time finite element methods for fluid-structure interaction in exterior domains, in: Comput. Meth. for Fluid/Structure Interaction, AMD, ASME 178 (1993) pp. 101–120.
[8] M.J. Grote, J.B. Keller, Exact NRBC for the time dependent wave equation, SIAM J. Appl. Math. 55 (1995) 280–297.
[9] M.J. Grote, J.B. Keller, NRBC for time-dependent scattering, J. Comput. Phys. 127 (1996) 52–65.
[10] H. Lamb, Hydrodynamics, 4th ed., Cambridge University Press, Cambridge, 1916, p. 517, Eq. 4.
[11] N.M. Newmark, A method of computation for structural dynamics, J. Eng. Mech. Div. ASCE (1959) 67–94.
[12] T.J.R. Hughes, A precis of developments in computational methods for transient analysis, J. Appl. Mech. 50 (1983) 1033–1040.
[13] J. Butcher, The Numerical Analysis of Ordinary Differential Equations, Wiley, New York, 1987.
[14] R.D. Cook, D.S. Malkus, M.E. Plesha, Concepts and Applications of Finite Element Analysis, 3rd ed., Wiley, New York, 1989.
[15] F.G. Friedlander, On the radiation field of pulse solutions of the wave equation, Proc. Roy. Soc. London A 269 (1962) 53–65.
[16] P.M. Morse, H. Feshbach, Methods of Theoretical Physics, vol. II, McGraw-Hill, New York, 1953.
[17] H.M. Hilber, T.J.R. Hughes, R.L. Taylor, Improved numerical dissipation for time-integration algorithms in structural mechanics, I. J. Earthquake Engrg. Structural Dynamics 5 (1977) 283–292.